Processing and Application of Ceramics 19 [4] (2025) 311–321
https://doi.org/10.2298/PAC2504311M

Design and characterization of CeO_2 nanoparticles with controlled morphology

Jelena Maletaškić[1,*], Marija Prekajski Djordjević[1], Nadežda Radmilović[2], Nina Daneu[3], Svetlana Butulija[1], Aleksandra Zarubica[4], Jelena Erčić[1], Branko Matović[1]

[1] *Centre of Excellence-CextremeLab Vinča, Institute of Nuclear Sciences Vinča, National Institute of the Republic of Serbia, University of Belgrade, Belgrade, Serbia*
[2] *Department of Atomics Physics, Institute of Nuclear Sciences Vinča, National Institute of the Republic of Serbia, University of Belgrade, Belgrade, Serbia*
[3] *Department for Advanced Materials, Jožef Stefan Institute, Ljubljana, Slovenia*
[4] *Faculty of Sciences and Mathematics, Department of Chemistry, University of Niš, Niš, Serbia*

Received 17 July 2025; Received in revised form 24 October 2025; Accepted 4 November 2025

Abstract

CeO_2 nanoparticles with isometric and rod-like morphologies were successfully synthesized through a simple hydrothermal method. The morphological evolution between isometric and nanorod morphologies was achieved by adjusting the concentration of NaOH, which affects the formation and morphological evolution of CeO_2 nanoparticles. The structure and properties of the CeO_2-xNaOH powders were characterized by powder X-ray diffraction, Raman spectroscopy, low temperature nitrogen adsorption, X-ray photoelectron spectroscopy, field-emission scanning electron microscopy and high-resolution transmission electron microscopy. Also, the ceria nanopowders were tested as a photocatalyst for the photodegradation of crystal violet dye in an aqueous solution. In summary, a straightforward and controllable approach for synthesizing CeO_2 nanoparticles with isometric and/or rod-like morphologies was demonstrated, utilizing simple starting materials in a hydrothermal system. The results present an economical method for synthesizing nanosized ceria and related materials. Additionally, understanding of the mechanism of morphology evolution provides new insights and strategies for the controlled synthesis of nanostructures.

Keywords: *ceria, hydrothermal synthesis, nanopowders, morphology-controlled growth*

I. Introduction

Over the last decade, there has been a significant progress in nanotechnology, particularly in the development of advanced functional nanomaterials with controlled sizes. Since many of their properties are size-dependent, modifying the morphology of nanomaterials can enhance their properties [1–8]. As a result, the synthesis of shape-controlled nanomaterials has become a key area of research, especially for rare earth oxides, which are known for their exceptional optical and catalytic properties and have broad applications [9–15].

Regarding photocatalysis, CeO_2-based nanomaterials exhibit excellent potential for the degradation of organic pollutants under UV or visible light [16,17]. The enhanced photocatalytic activity of CeO_2 nanostructures can be directly attributed to the formation and three-dimensional distribution of reactive oxygen species (ROS), such as hydroxyl (OH) and superoxide (O_2^-) radicals, which play a crucial role in the degradation of organic pollutants [18,19]. Surface defects like oxygen vacancies enhance photocatalytic efficiency by trapping electrons and extending charge carrier lifetimes [20]. Water pollution by synthetic dyes raises serious environmental and health risks due to their toxicity, persistence and potential carcinogenic effects [21]. CeO_2-based photocatalysts offer a promising solution, as they can efficiently degrade these pollutants through reactive oxygen species (ROS) generation while also enabling accurate monitoring of dye concentrations - essential for evaluating treatment efficiency and ensuring regulatory compliance [22].

* Corresponding author: +381 11 3408 224
e-mail: *jelena.pantic@vinca.rs*

Titanium dioxide (TiO_2) is widely used as a photocatalyst due to its stability and strong oxidizing ability; however, its wide band gap (~3.2 eV) limits activity to UV light, and rapid electron-hole recombination reduces efficiency. Additionally, TiO_2 shows low adsorption of organic pollutants, restricting practical applications [23]. CeO_2 nanomaterials offer advantages that overcome these drawbacks. Their Ce^{3+}/Ce^{4+} redox cycle creates oxygen vacancies that improve charge separation and extend light absorption into the visible region. Morphology control further enhances surface area and catalytic sites without complex doping [24]. These features make CeO_2 a promising alternative photocatalyst for degrading organic pollutants. A well-known example is CeO_2, which has remarkable abilities to store, release, and transport oxygen. CeO_2 exhibits defects that depend on the oxygen partial pressure. As the particle size decreases, ceria nanoparticles form more oxygen vacancies [25,26]. The large surface-to-volume ratio in nanoparticles enables CeO_2 to act catalytically, resulting in unique properties. Stoichiometric defects such as oxygen vacancies and their mobility on the oxide surface are crucial for redox reactions involving metal oxides with multiple oxidation states and are widely used in oxygen storage materials. Ceria (CeO_2) is one of the most important oxides in heterogeneous catalysis and is often used as a support material due to its redox properties [27–30]. The conductivity in nanocrystalline grain boundaries is higher than in larger grains, making it important to develop high-quality powders with nanoscale particle sizes.

Over the past decade, various CeO_2 nanostructures have been synthesized through different methods to investigate the relationship between size, morphology, and various properties [31–35]. In this work, nanosized CeO_2 was prepared using a simple hydrothermal method by employing different ceria morphologies (nanocubes, nano-octahedrons and nanorods). The hydrothermal synthesis is widely recognized as an effective one-step, low-temperature synthesis method. It is known for its ability to control powder reactivity and shape, making it one of the most efficient and cost-effective routes for synthesizing nanomaterials. The morphological evolution between nanocubes and nanorods was achieved by adjusting the concentration of NaOH, which played a key role in the formation and morphological evolution of CeO_2 nanostructures. Compared to bulk CeO_2, shape-controlled nano-CeO_2 shows significant improvements in structural and redox properties [36]. A range of advanced analytical techniques, such as scanning electron microscopy (SEM), high resolution transmission electron microscopy (HRTEM), energy dispersive X-ray spectroscopy (EDS), X-ray photoelectron spectroscopy (XPS), X-ray diffraction (XRD), Brunauer-Emmett-Teller (BET) surface area, Barrett-Joyner Halenda (BJH) pore analysis and Raman spectroscopy were used to analyse the physicochemical properties of the synthesized nanomaterials. The photocatalytic activity of ceria nanopowders was also evaluated by investigating the photodegradation of crystal violet (CV) dye in an aqueous solution.

II. Experimental

2.1. Synthesis procedure

Nanocrystalline CeO_2 was synthesized using cerium(III)-nitrate hexahydrate (Riedel-de Haën, 99% purity) and sodium hydroxide (Lach-Ner, 99% purity) as starting materials. The amounts of reactants used for synthesis of CeO_2 nanopowders were calculated according to the following equation:

$$2\,[Ce(NO_3)_3 \cdot 6\,H_2O] + 6\,NaOH + (1/2-\delta)O_2 \longrightarrow 2\,CeO_{2-\delta} + 6\,NaNO_3 + 9\,H_2O \qquad (1)$$

All used chemicals were of analytical grade and employed without further purification. Each sample contained 2.5 g of cerium(III)-nitrate hexahydrate ($Ce(NO_3)_3 \cdot 6\,H_2O$). Five samples with varying NaOH concentrations were prepared, starting from 0.7 g of NaOH for the lowest up to 14 g for the highest concentration (i.e. 1, 5, 10, 15 and 20 times more NaOH concentrated precursor solutions were used and corresponding samples were denoted as CeO_2-1NaOH, CeO_2-5NaOH, CeO_2-10NaOH, CeO_2-15NaOH and CeO_2-20NaOH, respectively). These chemicals were dissolved in 20 ml of distilled water by stirring, and then the mixture was transferred into a 40 ml Teflon liner. The initial pH of the solutions, depending on the NaOH concentration, ranged approximately from pH = 12 to 14. Distilled water was added to fill 80% of the total vial volume. The Teflon liner was placed inside a stainless-steel autoclave and maintained at 125 °C for 6 h, after which it was allowed to cool naturally to room temperature. The resulting precipitates were rinsed with distilled water in a centrifuge at 3500 rpm (5 times), followed by a rinse in alcohol, and then dried at 60 °C. After drying, the powders were observed to be yellow in colour.

2.2. Characterization techniques

All of the samples were characterized at room temperature by X-ray powder diffraction (XRPD) using an Ultima IV Rigaku diffractometer, equipped with Cu $K_{\alpha 1,2}$ radiation, using a generator voltage of 40.0 kV and a generator current of 40.0 mA. The range of 2θ = 20–80° was used for all powders in continuous scan mode with a scanning step size of 0.02° and at a scan rate of 2 °/min. Phase analysis was performed by using the PDXL2 software (version 2.0.3.0) [37], with reference patterns from the International Centre for Diffraction Data database (ICDD) [38], version 2012. All the structure information was taken from the American Mineralogist Crystal Structure Data Base [39].

The average crystallite size (D) was calculated based on the full-width at half-maximum intensity (FWHM) of the main reflections by applying Scherrer's formula:

$$D_{hkl} = \frac{K \cdot \lambda}{\beta \cdot \cos\theta} \tag{2}$$

where K is Scherrer's constant (~0.9), λ is wavelengths of the X-ray used, θ is the diffraction angle and β is the corrected half-width for instrumental broadening given as $\beta = (\beta_m - \beta_s)$ where β_m and β_s are the observed half-width and half-width of the standard ceria sample, respectively.

Internal lattice strain ($\Delta d/d$) of the calcined samples was estimated from the Williamson-Hall plots, using following equation [40]:

$$\beta_{total} \cos\theta = \frac{K \cdot \lambda}{D} + 4\frac{\Delta d}{d} \sin\theta \tag{3}$$

where β_{total} represents the full-width half-maximum of the characteristic XRD peak and Δd is the difference in the d spacing corresponding to a typical peak. The strain of nanocrystals, $\Delta d/d$, can be estimated from the slope of the function $\beta \cdot \cos\theta$ vs. $\sin\theta$ whereas the crystallite size, D, can be estimated from the y-intercept.

The morphology of the samples was investigated using scanning electron microscopy (SEM, JEOL JCM-5800 LV). For transmission electron microscopy observations, the samples were ultrasonically dispersed in pure ethanol and applied onto a holey carbon-coated copper grid. Prior to TEM analysis, the samples were additionally coated with a thin layer of carbon to prevent charging under the electron beam. TEM analyses were performed on a 200 kV microscope with a field emission gun (FEG) electron source (JEM-2010F, JEOL Ltd, Tokyo, Japan) and a Si(Li) energy-dispersive X-ray spectrometer (Link ISIS-300, Oxford Instruments, Oxfordshire, UK).

N_2 adsorption and desorption isotherms of the samples were measured at −196 °C. We used the gravimetric McBain method for the measurement of the specific surface area of materials. The specific surface area, S_{BET}, pore size distribution, mesopore surface area, including the external surface area, S_{meso}, and micropore volume, V_{mic}, of the samples were all calculated from the isotherms. Pore size distribution (PSD) was estimated by applying the Barrett-Joyner-Halenda (BJH) method [41] to the desorption branch of the isotherms, and mesopore surface area and micropore volume were estimated using the high resolution α_s plot method [42–44]. The increased surface area due to the presence of microporosity, S_{mic}, was calculated by subtracting S_{meso} from S_{BET}.

Unpolarized micro-Raman scattering measurements were performed in the backscattering configuration using a Jobin Yvon T64000 spectrometer equipped with a nitrogen cooled Symphony charge-coupled-device detector (CCD). As an excitation source, we used the 514.5 nm line of an Ar^+/Kr^+-ion laser operating at low power in order to avoid sample heating.

X-ray photoelectron spectroscopy was used for oxidation state and atomic ratio analyses. XPS analysis was performed using PHI Quantera equipment with a base pressure in the analysis chamber of 10^{-9} Torr. The X-ray source was monochromatized Al Kα radiation (1486.6 eV) and the energy resolution was 0.7 eV.

The photocatalytic activity of the synthesized CeO_2 nanopowders was studied using the degradation of the organic dye crystal violet (CV) as a test, under UV light irradiation, using 10 UV lamps (Roth Co, 16 W, 2.5 mW/cm^2, λ_{max} = 366 nm), each with a power of 28 W. The reaction was maintained at ambient temperature. The acidity of the solutions was not additionally adjusted, and pH values were in the range from 6.7 to 7.0. In this experiment, aqueous suspensions of the dye (initial concentration 0.01 mmol/dm^3) and 40 mg of the synthesized ceria powders were placed in a beaker. The volume of the test solution (the CV dye solution) was 0.05 dm^3. Prior to irradiation, the suspension was magnetically stirred in the dark for 1 h to ensure the establishment of the adsorption/desorption equilibrium. The suspension was kept under constant air-equilibrated conditions.

III. Results and discussion

The X-ray diffraction patterns of all the investigated powders, prepared with different NaOH concentrations, exclusively exhibit diffraction peaks corresponding to the CeO_2 fluorite-type structure, confirming that the powders are single-phase. No evidence of impurity phases was observed in any of the samples. The diffraction peaks show considerable broadening, which suggests the presence of small crystallite sizes and/or lattice strain. Additionally, the high background and low intensity of the reflections indicate that the crystallite size of the obtained samples is in the nanometre range. As the NaOH concentration increases, all the diffraction peaks shift to lower 2θ values, indicating an expansion of the unit cell. As shown in Fig. 1, the increasing NaOH concentration results in an increase in peak intensity and a decrease in the width of the diffraction lines, indicating an increase in crystallite size.

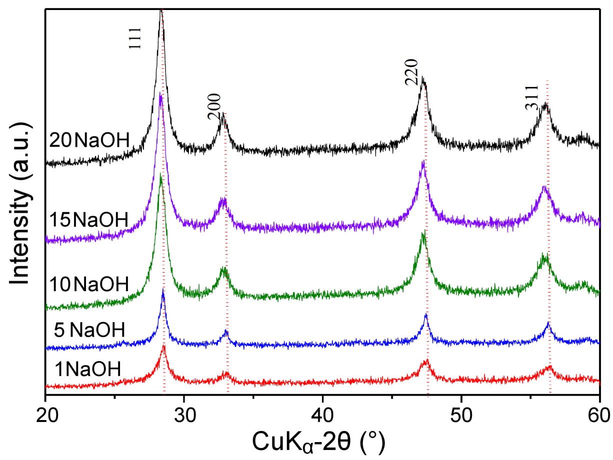

Figure 1. XRD spectra of CeO_2 samples synthesized with different concentrations of NaOH

Table 1. Lattice parameters, crystallite size and lattice strain of CeO_2 samples synthesized with different concentrations of NaOH determined from the XRD spectra

Sample	*a* [Å]	Crystallite size [nm]	Lattice strain, ε
CeO_2-1NaOH	5.4146(4)	10 ± 0.3	0.001842
CeO_2-5NaOH	5.4155(9)	10 ± 0.4	0.003676
CeO_2-10NaOH	5.4330(1)	11 ± 0.3	0.005713
CeO_2-15NaOH	5.4433(4)	12 ± 0.3	0.006099
CeO_2-20NaOH	5.4435(7)	14 ± 0.5	0.007789

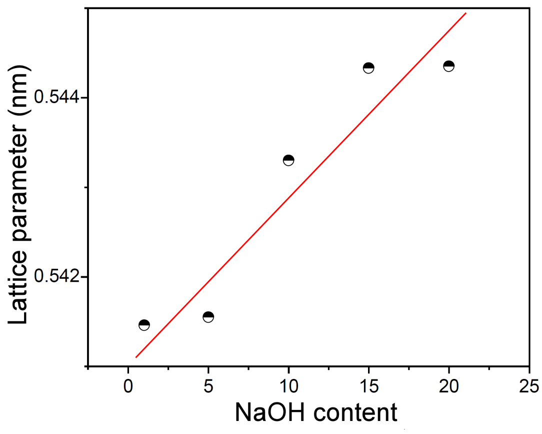

Figure 2. Lattice parameter of CeO_2 samples synthesized with different concentrations of NaOH

The values of crystallite size and lattice parameter for the samples prepared with different NaOH concentrations are presented in Table 1 and Fig. 2. Additionally, Table 1 includes the internal strain of the samples, which was estimated from the slope of the Williamson-Hall plots. The average crystallite size and lattice strain increase with the NaOH content, which is attributed to the distortion in the crystal lattice. The unit cell parameter of CeO_2 shows a linear dependence on the addition of NaOH [45]. It should be noted that the presence of Ce^{3+} introduces oxygen vacancies into the structure, which contributes to the lattice expansion and strain [46].

The Raman spectra of the CeO_2 samples are shown in Fig. 3. A distinct F_{2g} symmetry mode of the CeO_2 phase is observed around 462 cm^{-1}, which is attributed to the symmetrical stretching of the Ce–O vibrational unit in 8-fold coordination [47]. The peaks at 598 cm^{-1} are attributed to the defect-induced mode. The peak intensity of the defect-induced mode is influenced by the presence of defects in the ceria lattice, and it is enhanced when oxygen vacancies are present [48,49]. With increasing NaOH content, F_{2g} mode shifts to lower energies and becomes broader where some studies suggest that it is due to a higher concentration of oxygen vacancies. In the sample CeO_2-1NaOH, this mode is positioned at ~464 cm^{-1} and is more symmetric. In addition, the position of F_{2g} mode frequency for nanorods (~460 cm^{-1}) is lower than that for nanocubes, nanopolyhedra and the bulk (464 cm^{-1}) [50]. The F_{2g} mode, in the CeO_2 samples, shifts to lower frequencies and significantly broadens with an increase in NaOH concentration. Another mode, with lower intensity and positioned around 600 cm^{-1}, is assigned to the vibrations of defect complexes containing oxygen vacancies, which arise from the presence of Ce^{3+} ions commonly found in nano-ceria. This mode corresponds to the symmetrical stretching vibrations of the CeO_8 vibration unit and is highly sensitive to disorder in the oxygen sublattice [26,47]. The intensity of oxygen vacancy mode increases with NaOH content and is the highest for the sample CeO_2-20NaOH. The results indicate that the Ce^{3+} ions are concentrated on the surface, which leads to an increase in the number of oxygen vacancies [51]. These structural defects are known to increase photocatalytic activity by enabling charge carrier separation and promoting the formation of reactive oxygen species [17]. Moreover, the oxygen vacancies and surface-enriched Ce^{3+} ions act as active sites for adsorption and redox processes [52]. Thus, the Raman analysis confirms that these defects that are achieved by adjusting the NaOH concentration during the synthesis play a crucial role in optimizing the photocatalytic efficiency of CeO_2 nanostructures. The potential positions for reactive radicals (ROS) are typically at or near the oxygen vacancy sites. Oxygen vacancies, which are abundant in CeO_2 nanostructures, particularly those prepared with higher NaOH concentrations, act as the electron trapping centres, stabilize reduced Ce^{3+} sites, and promote the activation of O_2, thereby facilitating superoxide formation [16,20]. These processes are facilitated by the increased surface area and defect density, both of which are tunable through NaOH concentration during synthesis [19].

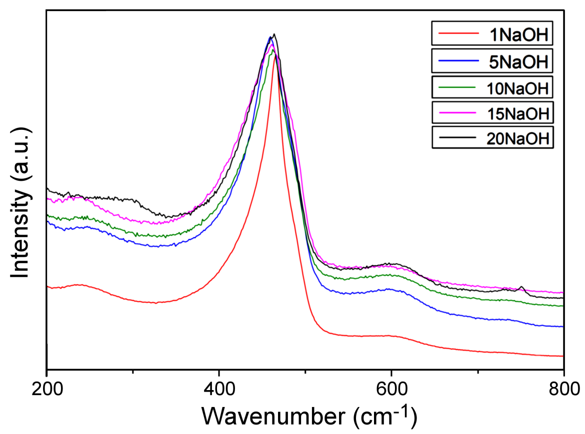

Figure 3. Raman spectra of CeO_2 samples synthesized with different NaOH concentration

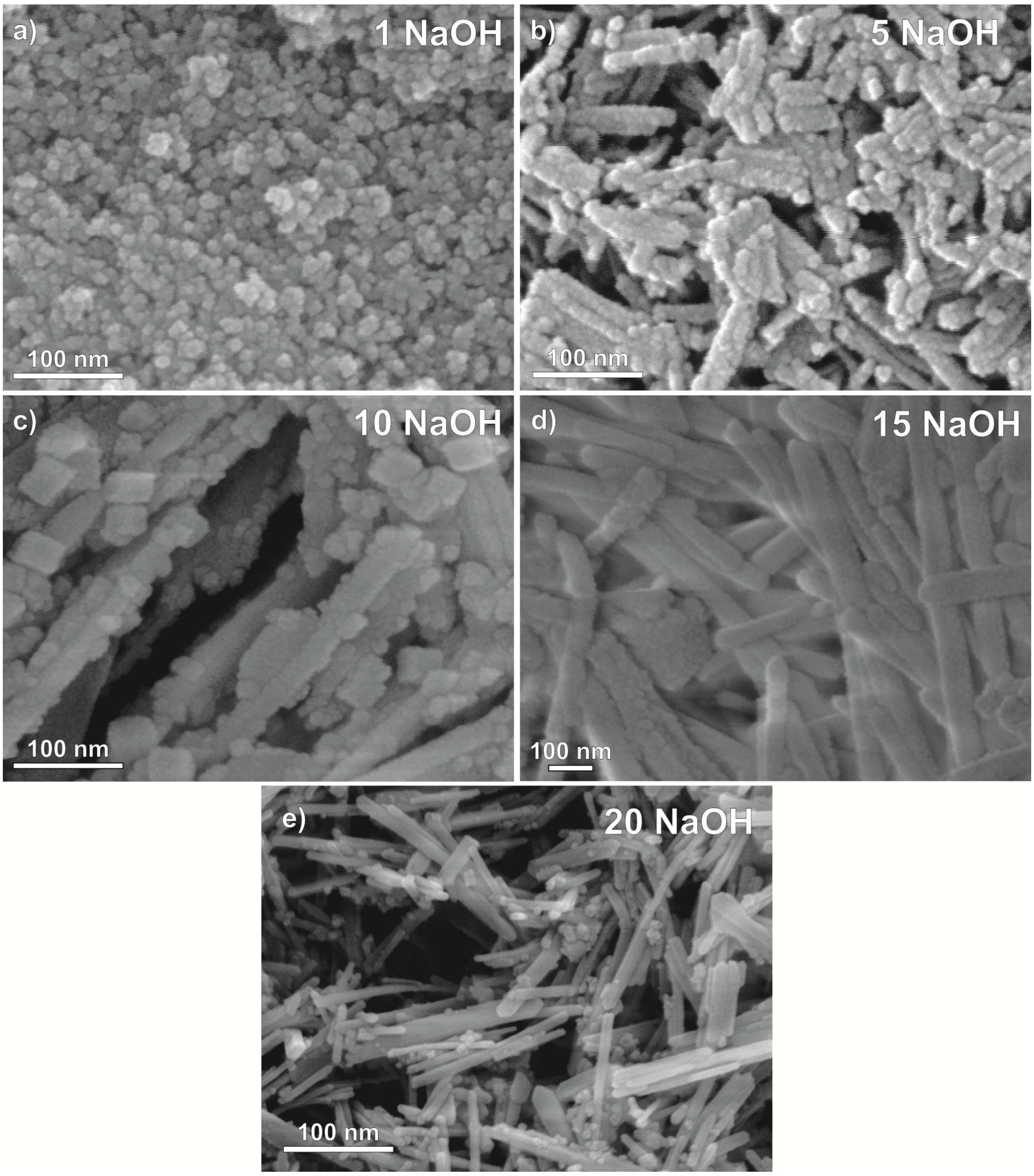

Figure 4. SEM images of CeO_2 particles obtained with different concentrations of NaOH: a) CeO_2-1NaOH sample presenting randomly agglomerated isometric nanoparticles, b) CeO_2-5NaOH with particles attached into rod-like formations, c) CeO_2-10NaOH forming larger clusters with isometric and rod-like morphology, d) CeO_2-15NaOH composed of rod-like particles with mostly rough surface and e) CeO_2-20NaOH sample composed of CeO_2 nanorods with high aspect ratio and smooth surface and some isometric particles attached to the surface

The effect of the reaction conditions on the morphology of the obtained samples was further investigated with electron microscopy. Figure 4 shows FESEM images of CeO_2 crystals obtained with different NaOH concentrations. It can be observed that all products contain particles in the nanoscale range.

With increasing amount of NaOH, the morphology of the crystals changes from isometric to elongated or rod-like. The lowest concentration of NaOH (Fig. 4a), results in the formation of agglomerated isometric nanoparticles. With the increase of NaOH concentration (the sample CeO_2-5NaOH), the isometric nanoparticles start to form elongated clusters of nanoparticles with lengths of up to 100 nm (Fig. 4b). The sample CeO_2-10NaOH prepared with an even higher NaOH addition is composed of clustered nanoparticles forming isometric and rod-like morphologies with larger sizes (Fig. 4c). A further increase in NaOH concentration (the sample CeO_2-15NaOH) results in the formation of rods with smoother surface and lower fraction of remaining nanoparticles (Fig. 4d). The effect is even more pronounced at the highest concentration of NaOH (Fig. 4e). This sample is composed of CeO_2 rods with smooth surface and much higher aspect ratio. In addition, the sample contains a low fraction of isometric CeO_2 nanoparticles attached to the surface of the nanorods.

For a better insight into the morphology of the formed nanoparticles and the influence of concentra-

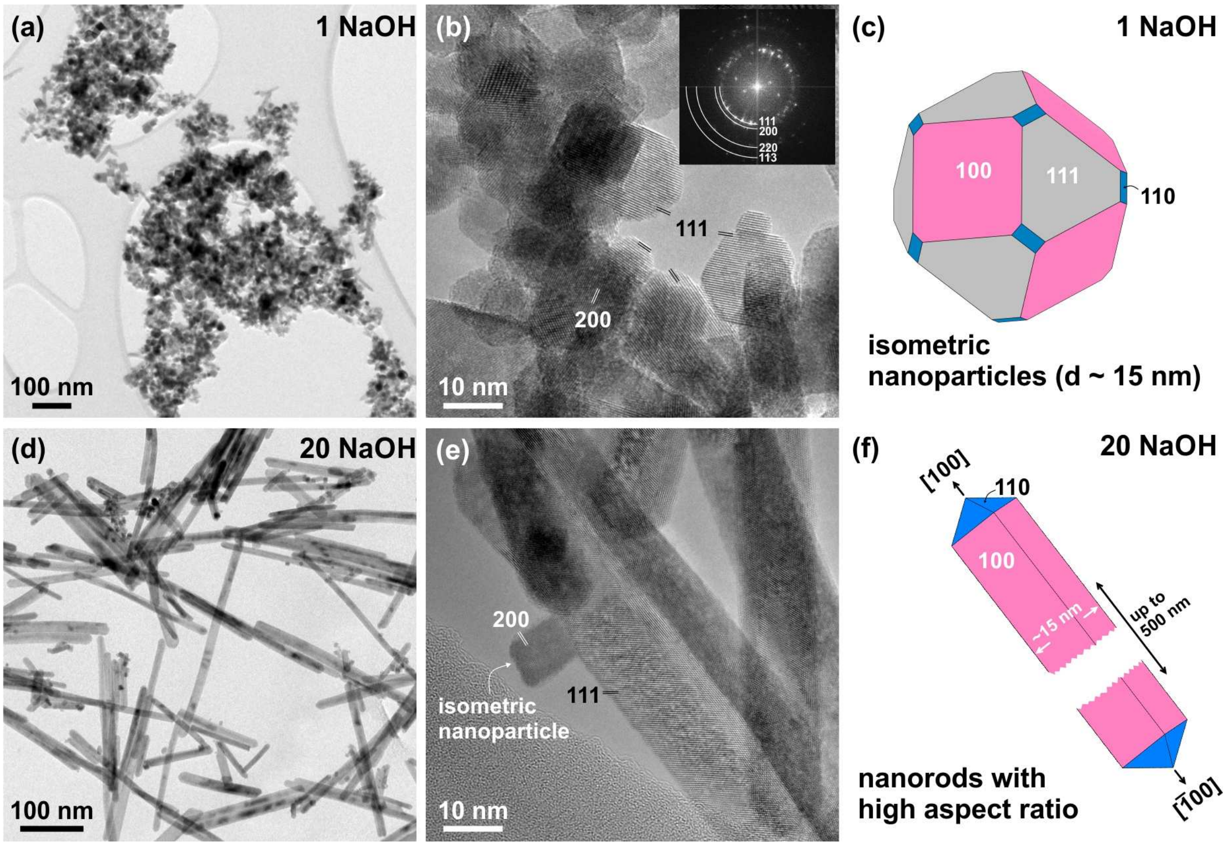

Figure 5. TEM analyses: a) typical CeO_2-1NaOH agglomerate, b) CeO_2-1NaOH cubes with measured $d_{(002)}$ = 0.273 nm, c) isomeric nanoparticle, d) CeO_2-20NaOH nanorods, e) magnified nanorods of CeO_2-20NaOH with $d_{(111)}$ = 0.311 nm and f) nanorod with high aspect ration

tion on their formation, the samples CeO_2-1NaOH and CeO_2-20NaOH were analysed by TEM (Fig. 5). A low-magnification TEM image of the sample CeO_2-1NaOH confirmed that it consists of agglomerated nanoparticles with isometric morphology (Fig. 5a). The average particle size determined from TEM images is between 9 and 21 nm, with an average particle size of 14 nm which is in good agreement with the results obtained by XRD measurements (Table 1). A high-resolution image of the nanoparticles is shown in Fig. 5b. Fast Fourier Transform (FFT) patterns show reflections from (111), (200), (110) and (113) lattice planes with d-values of 3.124, 2.706, 1.913 and 1.631 Å, respectively. Lattice fringes from the (111) and (200) planes are most commonly observed in the suitably oriented nanoparticles in the image. The nanoparticle morphology was reconstructed based on the analysis of edge-on-oriented facets (see Figure in Supporting Materials[§]) in differently oriented nanoparticles. The morphology of the isometric nanoparticles is presented in Fig. 5c and shows that the nanocrystals are enclosed by {111} and {100} facets of similar size and smaller {110} facets.

Figure 5d shows the typical morphology of the CeO_2-20NaOH sample consisting of nanorods with a high aspect ratio. The average diameter of the rods is around 15 nm, whereas their lengths can reach up to 500 nm. Figure 5e is a HRTEM image of an individual nanorod, not oriented in any low-index zone axis, however, the (111) lattice planes extending at an angle to the edge of the rod are well resolved. Detailed analysis of the crystal morphology revealed that the particles are elongated along the [001] direction, enclosed by {110} facets, and terminated by pyramidal {110} facets on both sides. A schematic presentation of a well-crystalized nanoparticle is shown in Fig. 5f. In addition to well-crystalized nanorods we also observed nanorods seemingly composed of oriented attached nanoparticle-domains.

To quantify the porosity of the samples, the nitrogen adsorption-desorption method was applied. The pore size distributions of the samples are shown in Fig. 6. Nitrogen adsorption/desorption isotherms for the samples at −196 °C are shown in the inset of Figs. 6a and 6b, as the amount of N_2 adsorbed as a function of relative pressure. Both samples have developed micro- and mesoporosity, with pore radii below 7 nm. According to the IUPAC classification [53], the isotherms are of type IV and have a hysteresis loop associated with mesoporous materials. In all samples, the shape of the hysteresis loop is type H4 which indicates narrow, slit pores [54]. The relatively high adsorption of nitrogen at a low relative pressure indicates the presence of a significant number of micropores in the samples. Specific surface areas, S_{BET}, calculated by the BET equation, are listed in Table 2. The S_{BET} values for the samples indicate that the specific surface area of the material rises with increasing molarity of the NaOH. α_s plots, obtained from the stan-

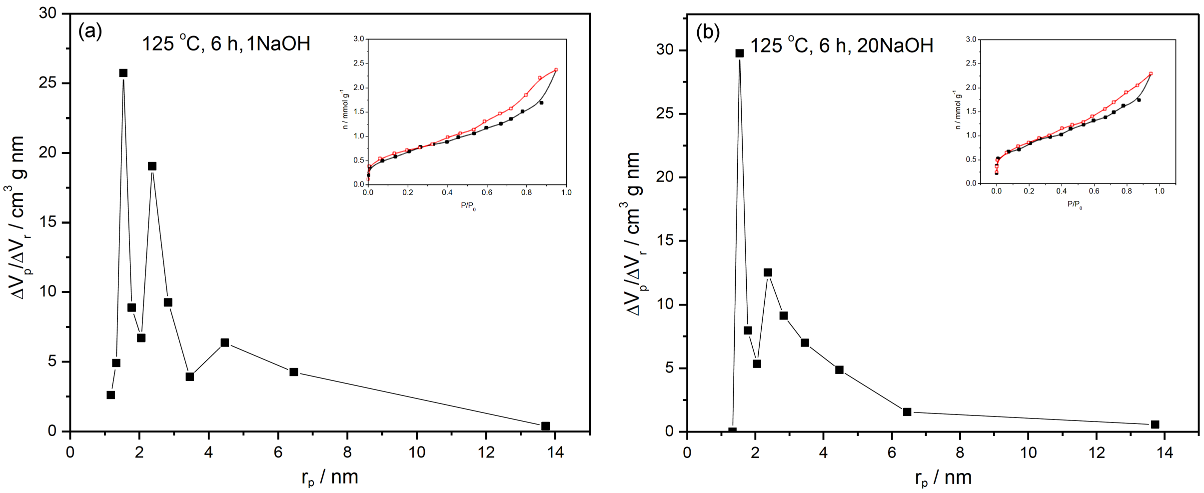

Figure 6. Pore size distribution (PSD) and nitrogen adsorption/desorption isotherms as function of relative pressure for: a) CeO_2-1NaOH and b) CeO_2-20NaOH samples synthesized with different concentration of NaOH

Table 2. Porous properties of CeO_2 samples synthesized with different NaOH content

Sample	S_{BET} [m²/g]	S_{meso} [m²/g]	S_{mic} [m²/g]	V_{mic} [cm³/g]
CeO_2-1NaOH (125 °C, 6 h)	58	55	3	0.002
CeO_2-20NaOH (125 °C, 6 h)	67	60	7	0.003

dard nitrogen adsorption isotherms, are shown in Fig. 7. The straight-line equation of the medium α_s region gives a mesoporous surface area including the contribution of the external surface, S_{meso}, from its slope, and the micropore volume, V_{mic}, from its intercept. The calculated porosity parameters (S_{meso}, S_{mic}, V_{mic}) are given in Table 2. Analysis of the experimental data confirms that both samples are predominantly mesoporous, and that the specific surface, as well as micropore area, increase with increasing molar ratio of NaOH.

Figure 8 shows the Ce 3d XPS spectra of the CeO_2 samples synthesized with different NaOH contents. The spectra were fitted using the Gaussian-Lorentzian profiles, and the overall fit is presented for all samples. Six peaks corresponding to the pairs of spin-orbit doublets can be identified in the Ce $3d_{3/2,5/2}$ spectrum (CeO_2), which is in good agreement with the literature [55–57]. The deconvolution of the spectra yields four spin-orbit doublets ($3d_{5/2}$ and $3d_{3/2}$) labelled v–v^{000} and u–u^{000} using the notation of Ce peaks introduced by Burroughs [45] and a small extra satellite feature labeled as t, which could be a contribution from a multiplet splitting effect. The position of the peaks and their binding energies (BE) are summarized in Table 3. Doublets u/v, u^{00}/v^{00} and u^{000}/v^{000} belong to Ce^{4+}, while u^0/v^0 belongs to Ce^{3+}. Based on peak intensity, it can be seen that the relative concentration of Ce^{3+} ions is almost constant, while the concentration of Ce^{4+} is decreas-

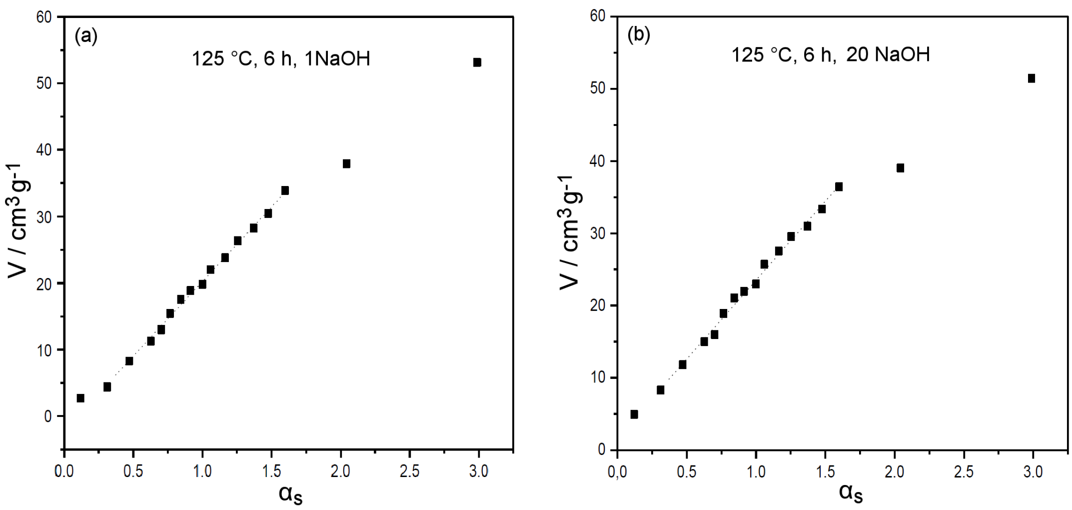

Figure 7. α_s-plots for nitrogen adsorption isotherm of: a) CeO_2-1NaOH and b) CeO_2-20NaOH samples synthesized with different NaOH content

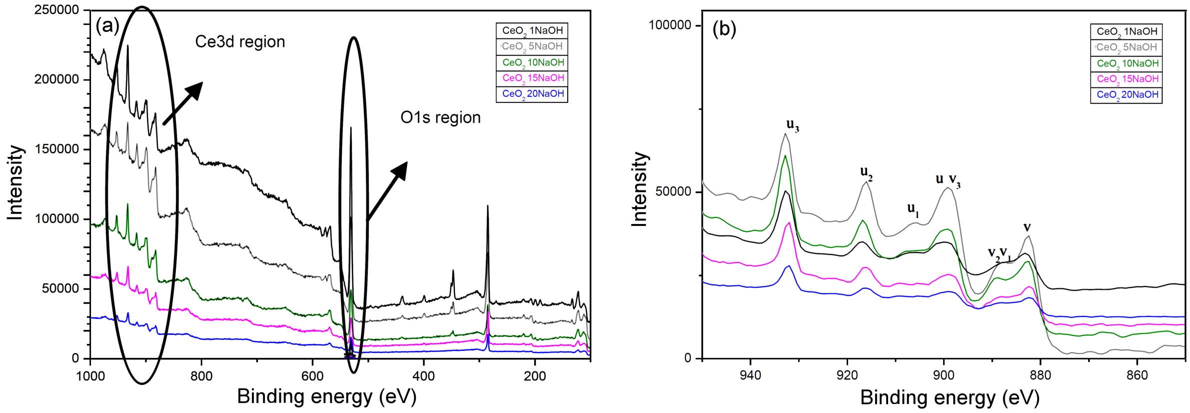

Figure 8. XPS survey spectra of the CeO_2 samples synthesized with different NaOH content (a) and the Ce $3d_{3/2,5/2}$ core level spectrum (b)

Table 3. Binding energies (eV) of individual peaks in the Ce 3*d* spectrum for several nanocrystalline samples

Sample	$3d_{5/2}$				$3d_{3/2}$			
	v	v'	v''	v'''	u	u'	u''	u'''
CeO_2-1NaOH	882.7	887.2	888.1	897.0	899.1	905.1	916.2	932.8
CeO_2-5NaOH	882.5	887.5	888.2	897.1	899.2	905.1	916.3	932.7
CeO_2-10NaOH	882.9	887.2	888.0	897.1	899.4	905.5	916.7	932.5
CeO_2-15NaOH	882.4	887.4	888.5	897.3	899.7	905.8	916.8	932.2
CeO_2-20NaOH	882.0	887.5	888.6	897.5	899.9	905.9	916.1	932.1

ing. It is important to note that these values correspond to the surface layer of the samples, approximately 1 nm in thickness, which is the most sensitive layer for XPS analysis. The O 1*s* region of the XPS spectra is presented in Fig. 8b. It can be seen that the O_{HBE} peak decreases with NaOH content. This peak is associated with the presence of oxygen vacancies [58–60]. The O 1*s* core-level peak from the lattice oxygen in CeO_2 was detected at about 529.8 ± 0.1 eV. For Ce^{3+} compounds, the O 1*s* core level peak shifts to higher binding energy at 531.5 ± 0.1 eV (+1.7 eV). This shift is due to the presence of Ce^{3+} states [61,62]. No hydroxide species were detected. Therefore, the decrease in the O peak with increasing NaOH content reflects an increase in oxygen vacancies concentration, which is in complete agreement with our previous XRD and Raman scattering analyses.

Figure 9 shows the C/C_0 values of the ceria nanopowders over time, where C represents the absorbance of the CV aqueous solution with ceria nanopowders after UV irradiation for a given time t, and C_0 is the initial absorbance of the CV solution before the addition of ceria samples. From the figure, it is evident that C/C_0 decreases as time progresses. After 360 min, the sample CeO_2-5NaOH shows the highest photocatalytic activity (94%), followed closely by the CeO_2-1NaOH sample. This enhanced activity can be attributed to the larger specific surface area of these samples. The lower photocatalytic activity observed in other samples can be explained by their different morphologies, which likely affect their

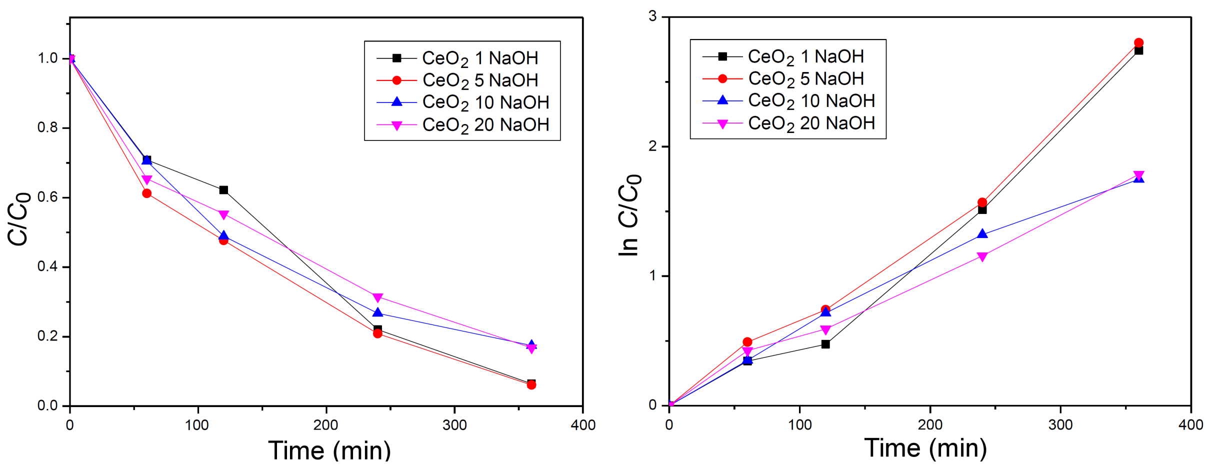

Figure 9. Kinetics of photocatalytic degradation of CV by the ceria nanopowders

surface reactivity and efficiency in the photocatalytic process. When compared with the pure CeO_2 [63,64], which shows little or no photocatalytic activity, the properties of CeO_2 nanoparticles can be significantly improved without the need for additional dopants or external modifications, and simply through morphology control alone. To further understand the photocatalytic degradation behaviour, the kinetics of crystal violet dye decomposition was analysed using the pseudo-first-order model by plotting $\ln(C_0/C)$ versus time (Fig. 9). The data exhibited good linearity, indicating that the degradation follows pseudo-first-order kinetics [65]. The apparent rate constant kapp for the CeO_2-5NaOH sample was calculated to be $0.0076\,\text{min}^{-1}$, the highest among all samples tested. This suggests more efficient charge separation and higher availability of active sites. This alignment of experimental kinetics with the Hinshelwood model [66] underlines the crucial role of surface adsorption and morphology (surface area, oxygen vacancies) in governing the photocatalytic efficiency of CeO_2 nanostructures.

IV. Conclusions

CeO_2 nanocubes and nanorods were successfully prepared through a simple hydrothermal method, by adjusting the NaOH concentration. The phase identified by XRD was single-phase CeO_2 and all the diffraction peaks for each sample were significantly broadened, indicating small crystallite size and/or strain. As it can be seen from XPS results, based on peak intensity, the relative concentration of Ce^{3+} ions remained nearly constant, while that of Ce^{4+} decreased. Also, the decrease of the O peak with increasing NaOH content reflects a rise in oxygen vacancies concentration, which is in full agreement with XRD and Raman scattering analyses. BET analysis confirms that all samples are predominantly mesoporous, and that both specific surface and micropore area increase with higher NaOH molarity. The photocatalytic ability of the synthesized CeO_2 nanopowders showed that it can be enhanced without any dopants, simply through morphology control.

Acknowledgement: This research was financially supported by the Ministry of Science, Technological Development and Innovation of the Republic of Serbia (Grant Nos. 451-03-136/2025-03/200017). This work has been enabled through the Slovenian-Serbian bilateral collaboration under the project No. BI-RS/12-13-019: Minerals as precursors for advanced technologies. One of the authors Branko Matović, as well as Jelena Maletaškić, gratefully acknowledges the financial support from the Tokyo Institute of Technology, Laboratory for Advanced Nuclear Energy, Institute of Innovative Research, as visiting professors.

References

1. Z.Y. Zhou, N. Tian, J.T. Li, I. Broadwell, S.G. Sun, "Nanomaterials of high surface energy with exceptional properties in catalysis and energy storage", *Chem. Soc. Rev.*, **40** (2011) 4167–4185.
2. G. Osama, M.Z. Khan, I. Bibi, N. Bashir, U. Tariq, M. Bakhtiar, M.R.A. Karim, F. Ali, M.B. Hanif, M. Motola, "Nanomaterials for advanced energy applications: Recent advancements and future trends", *Mater. Des.*, **241** (2024) 112930.
3. S. Sultana, S. Mansingh, K.M. Parida, "Crystal facet and surface defect engineered low dimensional CeO_2 (0D, 1D, 2D) based photocatalytic materials towards energy generation and pollution abatement", *Mater. Adv.*, **2** (2021) 6942–6983.
4. D. Zhang, X. Du, L. Shia, R. Gao, "Shape-controlled synthesis and catalytic application of ceria nanomaterials", *Dalton Trans.*, **41** (2012) 14455–14475.
5. C. Dong, Y. Zhou, N. Ta, W. Shen, "Formation mechanism and size control of ceria nanocubes", *Cryst. Eng. Comm.*, **22** (2020) 3033–3041.
6. H. Yang, L. Jia, J. Haraguchi, Y. Wang, B. Xu, Q. Zhang, Z. Nan, M. Zhang, T. Ohno, "Nitrogen and sulfur co-doped CeO_2 nanorods for efficient photocatalytic VOCs degradation", *Catal. Sci. Technol.*, **12** (2022) 5203–5209.
7. A.E. D'Achille, R.M. Wallace, J.L. Coffer, "Morphology-dependent fluorescence of europium-doped cerium oxide nanomaterials", *Nanoscale Adv.*, **3** (2021) 3563–3572.
8. Y. Li, W. Shen, "Morphology-dependent nanocatalysts: Rod-shaped oxides", *Chem. Soc. Rev.*, **43** (2014) 1543–1574.
9. A. Othman, A. Gowda, D. Andreescu, M.H. Hassan, S.V. Babu, J. Seo, S. Andreescu, "Two decades of ceria nanoparticle research: structure, properties and emerging applications", *Mater. Horiz.*, **11** (2024) 3213–3266.
10. S. Gao, D. Yu, S. Zhou, C. Zhang, L. Wang, X. Fan, X. Yu, Z. Zhao, "Construction of cerium-based oxide catalysts with abundant defects/vacancies and their application to catalytic elimination of air pollutants", *J. Mater. Chem. A*, **11** (2023) 19210–19243.
11. P.K. Sharma, O.P. Pandey, "Synthesis and catalytic study of CeO_2 heterostructures with $(Zn_{0.003\text{-}x}Cd_x)S_{0.003}$ for the removal of crystal violet dye", *Phys. Rev. B Condens.*, **631** (2022) 413702.
12. G. Vimal, K.P. Mani, P.R. Biju, C. Joseph, N.V. Unnikrishnan, M.A. Ittyachen, "Influences of annealing temperature and doping concentration on microstructural and optical properties of CeO_2:Sm^{3+} nanocrystals", *Acta Metall. Sin.*, **28** (2015) 758–765.
13. B. Chen, J. Qiu, L. Xu, Y. Cui, "Ni-based mesoporous $Ce_{0.8}Zr_{0.2}O_2$ catalyst with enhanced low-temperature performance for CO_2 methanation", *Catal. Commun.*, **171** (2022) 106515.
14. Y.H. Liu, C.Q. Yin, L.H. Wang, D.B. Li, J.S.Lian, J.D. Hu, Z.X. Guo, "Properties of a ceria-based $(C_6S_2G_2)$ solid oxide electrolyte sintered with Al_2O_3 additive", *Sci. Sinter.*, **40** (2008) 13–20.
15. A.A. Ansari, J.P. Labis, M. Alam, S.M. Ramay, N. Ahmat, A. Mahmood, "Synthesis, structural and optical properties of Mn-doped ceria nanoparticles: a promising catalytic material", *Acta Metall. Sin.*, **29** (2016) 265–273.
16. A.A. Fauzi, A.A. Jalil, N.S. Hassan, F.F.A. Aziz, M.S. Azami, I. Hussain, R. Saravanan, D.-V.N. Vo, "A critical review on relationship of CeO_2-based photocatalyst towards mechanistic degradation of organic pollutant", *Chemosphere*, **286** (2022) 131651.

17. Y. Lan, X. Xia, J. Li, X. Mao, C. Chen, D. Ning, Z. Chu, J. Zhang, F. Liu, "Insight into the contributions of surface oxygen vacancies on the promoted photocatalytic property of nanoceria", *Nanomaterials*, **11** (2021) 1168.
18. R. Ma, S. Zhang, L. Li, P. Gu, T. Wen, A. Khan, S, Li, B. Li, S. Wang, X. Wang, "Enhanced visible-light-induced photoactivity of type-II CeO_2/g-C_3N_4 nanosheet toward organic pollutants degradation", *ACS Sustain. Chem. Eng.*, **7** [10] (2019) 9699–9708.
19. J. Pan, S. Wang, A. Chen, Y. Chen, M. Wang, Y. Chen, "Visible-light-active mesoporous ceria (CeO_2) nanospheres for improved photocatalytic performance", *J. Alloys Compd.*, **898** (2022) 162895.
20. D. Yang, Y. Xia, L. Zhang, J. Liu, X. Zhu, W. Feng, "Investigation on the structural and photocatalytic performance of oxygen-vacancy-enriched SnO_2-CeO_2 heterostructures", *Int. J. Mol. Sci.*, **24** (2023) 15446.
21. E. Forgacs, T. Cserháti, G. Oros, "Removal of synthetic dyes from wastewaters: a review", *Environ. Int.*, **30** (2004) 953–971.
22. V. Madaan, B. Mohan, V. Bhankar, R. Ranga, P. Kumari, P. Singh, M. Sillanpää, A. Kumar, A.A. Solovev, K. Kumar, "Metal-decorated CeO_2 nanomaterials for photocatalytic degradation of organic pollutants", *Inorg. Chem. Commun.*, **146** (2022) 110099.
23. S. Mirsalari, A. Nezamzadeh-Ejhieh, A. Massah, "A designed experiment for CdS-AgBr photocatalyst toward methylene blue", *Environ. Sci. Pollut. Res.*, **29** (2022) 33013–33032.
24. A. Trovarelli, "Catalytic properties of ceria and CeO_2-containing materials", *Catal. Rev.*, **38** (1996) 439–520.
25. M. Prekajski, Z. Dohčević-Mitrović, M. Radović, B. Babić, J. Pantić, A. Kremenović, B. Matović, "Nanocrystaline solid solution CeO_2-Bi_2O_3", *J. Eur. Ceram. Soc.*, **32** (2012) 1983–1987.
26. Z. Dohcevic-Mitrovic, M.J. Scepanovic, M.U. Grujic-Brojcin, Z.V. Popovic, S. Boskovic, B. Matovic, M.V. Yinkevich, F. Aldinger, "The size and strain effects on the Raman spectra of $Ce_{1-x}Nd_xO_{2-\delta}$ ($0 \leq x \leq 0.25$) nanopowders", *Solid State Commun.*, **137** (2006) 387–390.
27. E. Martín Morales, A. Alarcón, M. Biset-Peiró, E. Xuriguera, J. Guilera, "Shaping of porous CeO_2 powders into highly active catalyst carriers", *ACS Appl. Eng. Mater.*, **1** (2023) 1106–1115.
28. J.D. Jiménez, L.E. Betancourt, M. Danielis, H. Zhang, F. Zhang, I. Orozco, W. Xu, J. Llorca, P. Liu, A. Trovarelli, J.A. Rodríguez, S. Colussi, S.D. Senanayake, "Identification of highly selective surface pathways for methane dry reforming using mechanochemical synthesis of Pd-CeO_2", *ACS Catal.*, **12** (2022) 12809–12822.
29. B. Matović, J. Dukić, A. Devečerski, S. Bošković, M. Ninić, Z. Dohčević-Mitrović, "Crystal structure analysis of Nd-doped ceria solid solutions", *Sci. Sinter.*, **40** (2008) 63–68.
30. S. Liu, X. Liao, Q. Zhang, Y. Zhang, H. Wang, Y. Zhao, "Crystal-plane and shape influences of nanoscale CeO_2 on the activity of Ni/CeO_2 catalysts for maleic anhydride hydrogenation", *Nanomaterials*, **12** (2022) 762.
31. G.V. Ashok Reddy, H. Shaik, K.N. Kumar, H.D. Shetty, R.I. Jafri, R. Naik, J. Gupta, S.A. Sattar, B.H. Doreswamy, "Synthesis, characterizations, and electrochromic studies of WO_3 coated CeO_2 nanorod thin films for smart window applications", *Phys. Rev. B Condens.*, **647** (2022) 414395.
32. P.P. Ortega, R.A.C. Amoresi, M.D. Teodoro, L.G. Merízio, M.A. Ramirez, C.M. Aldao, C. Malagù, M.A. Ponce, E. Longo, A.Z. Simões, "Insights into the morphology and structural defects of Eu-doped ceria nanostructures for optoelectronic applications in red-emitting devices", *ACS Appl. Nano Mater.*, **7** (2024) 12466–12479.
33. Y. Choi, J. Kim, H.G. Seo, H.L. Tuller, W.C. Jung, "Nucleation and growth kinetics of electrochemically deposited ceria nanostructures for high-temperature electrocatalysis", *Electrochim. Acta*, **316** (2019) 273–282.
34. T.A. Knecht, J.E. Hutchison, "Reaction atmospheres and surface ligation control surface reactivity and morphology of cerium oxide nanocrystals during continuous addition synthesis", *Inorg. Chem.*, **61** (2022) 4690–4704.
35. J. Maletaškić, M. Cebela, M. Prekajski Djordjevic, D. Kozlenko, S. Kichanov, M. Mitric, B. Matovic, "Combined magnetic and structural characterization of hidrothermal bismuth ferrite ($BiFeO_3$) nanoparticles", *Sci. Sinter.*, **51** (2019) 71–79.
36. C. Sun, H. Li, L. Chen, "Nanostructured ceria-based materials: Synthesis, properties, and applications", *Energy Environ. Sci.*, **5** (2012) 8475–8505.
37. PDXL, Version 2.0.3.0 Integrated X-ray powder diffraction software, Rigaku Corporation, Tokyo (Japan), 2011, 196-8666.
38. S. Gates-Rector, T. Blanton, "The powder diffraction file: a quality materials characterization database", *Powder Diffr.*, **34** (2019) 352–360.
39. R.T. Downs, M. Hall-Wallace, "The American mineralogist crystal structure database", *Am. Mineral.*, **88** (2003) 247–250.
40. J. Rodríguez-Carvajal, "Recent advances in magnetic structure determination by neutron powder diffraction", *Physica B*, **192** (1993) 55–59.
41. E.P. Barrett, L.G. Joyner, P.P. Halenda, "The determination of pore volume and area distributions in porous substances. I. Computations from nitrogen isotherms", *J. Am. Ceram. Soc.*, **73** (1951) 373–380.
42. K. Kaneko, C. Ishii, M. Ruike, H. Kuwabara, "Origin of superhigh surface area and microcriystalline graphitic structures of activated carbons", *Carbon*, **30** (1992) 1075–1088.
43. K. Kaneko, C. Ishii, H. Kanoh, Y. Hanzawa, N. Setoyama, T. Suzuki, "Characterization of porous carbons with high resolution α_s-analysis and low temperature magnetic susceptibility", *Adv. Colloid Interface Sci.*, **76-77** (1998) 295–320.
44. M. Kruk, M. Jaroniec, K.P. Gadakaree, "Nitrogen adsorption studies of novel synthetic active carbons", *J. Colloid Interface Sci.*, **192** (1997) 250–256.
45. Z. Dohčević-Mitrović, S. Aškrabić, B.S. Stojadinović, D.M. Djokić, "Temperature-dependent Raman spectroscopy for nanostructured materials characterization" Chapter 2, pp. 11–44 in *Micro and Nano Technologies, Design, Fabrication, and Characterization of Multifunctional Nanomaterials*. Eds. S. Thomas, N. Kalarikkal, A.R. Abraham. Elsevier, Amsterdam, The Netherlands, 2022.
46. X. Wang, N. Wang, Z. Zhang, X. Tan, Y. Zheng, J. Yang, "Controlled synthesis of triangular submicron-sized CeO_2 and its polishing performance", *Materials*, **17** (2024) 2001.
47. A. El-Habib, B. Brioual, J. Zimou, Z. Rossi, A. Marjaoui, M. Zanouni, A. Aouni, M. Jbilou, M. Diani, M. Addou,

"Comparative studies on the structural, optical and electrochemical properties of Gd, Nd and In-doped CeO_2 nanostructured thin films", *Mater. Sci. Semicond. Process.*, **176** (2024) 108287.

48. R. Venkataswamy, L. Trimble, S. Ryu, N.-T. Le, K. Park, H. Kang, J. Seo, "Atomic-level insights into CeO_2 performance: chemical interactions in CMP explored through CeO_2-SiO_2 studies", *Ceram. Int.*, **50** (2024) 46032–46041.
49. S. Loridant, "Raman spectroscopy as a powerful tool to characterize ceria-based catalysts", *Catal. Today*, **373** (2021) 98–111.
50. W.H. Weber, K.C. Hass, J.R. McBride, "Raman study of CeO_2: Second-order scattering, lattice dynamics, and particle-size effects", *Phys. Rev. B*, **48** (1993) 17–85.
51. P. Dutta, S. Pal, M. S. Seehra, "Concentration of Ce^{3+} and oxygen vacancies in cerium oxide nanoparticles", *Chem. Mater.*, **18** (2006) 5144–5146.
52. M. Yang, G. Shen, Q. Wang, K. Deng, M. Liu, Y. Chen, Y. Gong, Z. Wang, "Roles of oxygen vacancies of CeO_2 and Mn-doped CeO_2 with the same morphology in benzene catalytic oxidation", *Molecules*, **26** (2021) 6363.
53. K.S.W. Sing, D.H. Everett, R.A.W. Haul, L. Moscou, R.A. Pierotti, J. Rouquerol, T. Siemieniewska, "Reporting physisorption data for gas/solid systems with special reference to the determination of surface area and porosity", *Pure Appl. Chem.*, **57** (1985) 603–619.
54. S. Lowell, J.E. Shields, M.A. Thomas, M. Thommes, *Characterization of Porous Solids and Powders: Surface Area, Pore Size and Density*, Kluwer Academic Publishers, Dordrecht Netherlands, 2004, p. 44.
55. P. Burroughs, A. Hamnett, A.F. Orchard, G.J. Thornton, "Satellite structure in the X-ray photoelectron spectra of some binary and mixed oxides of lanthanum and cerium", *Chem. Soc. Dalton Trans.*, **17** (1976) 1686–1698.
56. C.M. Sims, R.A. Maier, A.C. Johnston-Peck, J.M. Gorham, V.A. Hackley, B.C. Nelson, "Approaches for the quantitative analysis of oxidation state in cerium oxide nanomaterials", *Nanotechnology*, **30** (2019) 085703.
57. R. Shao, L. Zhang, L. Wang, J. Wang, X. Zhang, S. Han, X. Cheng, Z. Wang, "Cerium oxide-based catalyst for low-temperature and efficient ammonia decomposition for hydrogen production research", *Int. J. Hydrogen Energy.*, **68** (2024) 311–320.
58. L.R. Shah, A. Bakhtyar, Z. Hao, W.G. Wang, Y.Q. Song, H.W. Zhang, S.I. Shah, J.Q. Xiao, "Detailed study on the role of oxygen vacancies in structural, magnetic and transport behavior of magnetic insulator: Co-CeO_2", *J. Phys. Condens. Matter.*, **21** (2009) 486004.
59. T. Bao, H. Zhou, Y. Zhang, C. Guo, W. Guo, H. Qin, P. Gao, H. Xiao, W. Liu, "Effect of CeO_2 on carbon deposition resistance of Ni/CeO_2 catalyst supported on SiC porous ceramic for ethanol steam reforming", *J. Rare Earths*, **41** (2023) 1703–1713.
60. X. Mao, X. Xia, J. Li, C. Chen, X. Gu, S. Li, Y.-P. Lan, "Self-assembly of structured $CeCO_3OH$ and its decomposition in H_2 for a novel tactic to obtain CeO_{2-x} with excellent photocatalytic property", *J. Alloys Compd.*, **870** (2021) 159424.
61. D.R. Mullins, S.H. Overbury, D.R. Huntley, "Electron spectroscopy of single crystal and polycrystalline cerium oxide surfaces", *Surf. Sci.*, **409** (1998) 307–319.
62. F. Larachi, J. Pierre, A. Adnot, A. Bernis, "Ce 3d XPS study of composite $Ce_xMn_{1-x}O_{2-y}$ wet oxidation catalysts", *Appl. Surf. Sci.*, **195** (2002) 236–250.
63. B. Matovic, J. Lukovic, B. Stojadinovic, S. Askrabic, A. Zarubica, B. Babic, Z. Dohcevic-Mitrovic, "Influence of Mg doping on structural, optical and photocatalytic performances of ceria nanopowders", *Process. Appl. Ceram.*, **11** (2017) 304–310.
64. Y.-S. Li, A. Fang, G.-J. Lee, J.J. Wu, Y.-C. Chang, C.-Y. Tsay, J.-H. Chen, T.-L. Horng, C.-Y. Chen, "Properties of heterostructured ceria/polyaniline nanoparticles", *Catalysts*, **10** (2020) 732.
65. L. Bai, S. Wang, Z. Wang, E. Hong, Y. Wang, C. Xia, B. Wang, "Kinetics and mechanism of photocatalytic degradation of methyl orange in water by mesoporous Nd-TiO_2-SBA-15 nanocatalyst", *Environ. Pollut.*, **248** (2019) 516–525
66. E. Riedal, "The kinetics of chemical change", *Nature*, **146** (1940) 603–604.